Supplementary information

Interfacial Potential Transduction for Diagnostics

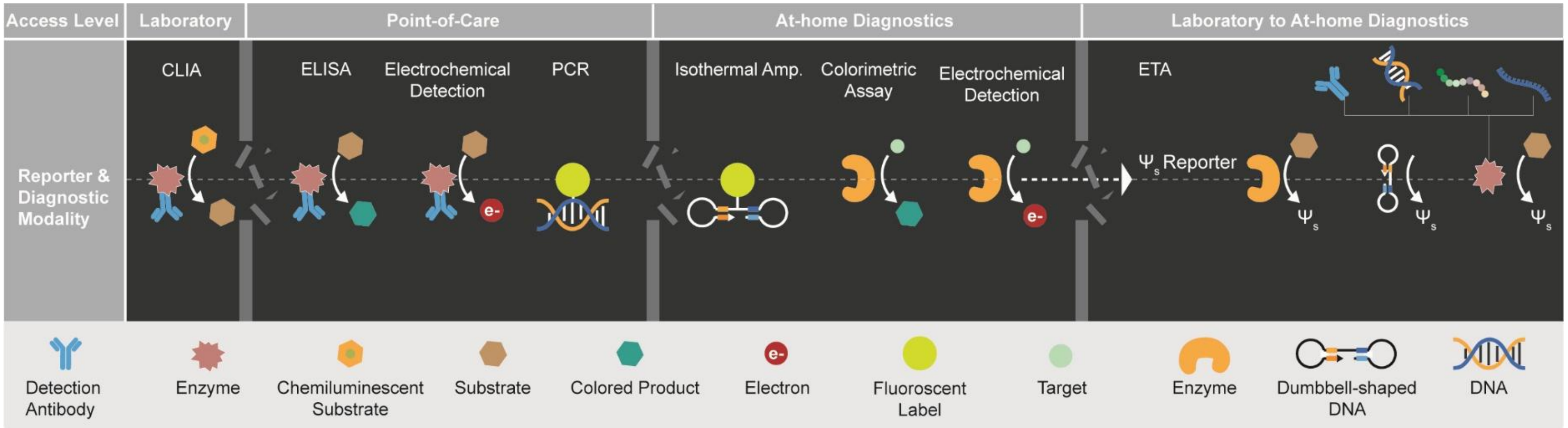

Supplementary Information Fig. 1. Landscape of diagnostic signal transduction across accessibility and analytical performance. Across biochemical analysis, immunoassays, and molecular diagnostics, signal transduction has largely relied on reporters that generate measurable outputs. Optical reporters produce light signals from biological binding events, commonly through enzyme reactions or fluorescent labels. Electrochemical reporters generate measurable electrical signals (electrons), typically through enzyme-mediated redox reactions—together representing the two dominant physical vectors used in diagnostic readouts: photons and electrons. Highly sensitive chemiluminescent immunoassays (CLIA), which rely on transient light emission from enzyme–substrate reactions, require high-sensitivity optical instrumentation integrated with automated processing and are therefore predominantly implemented in centralized laboratories[1]. The enzyme-linked immunosorbent assay (ELISA), a widely adopted standard in immunoassays, detects enzyme-generated colorimetric signals and has been adapted for point-of-care use[2]; however, reliance on optical readers and challenges in reagent stability continue to limit miniaturization. Electrochemical detection approaches enable compact transduction system, but their performance can be influenced by matrix effects and electrode variability[3]. In molecular diagnostics, polymerase chain reaction (PCR) remains a reference method by monitoring optical signals during thermal cycling, though its instrumentation requirements limit portability[4]. Isothermal amplification methods reduce system complexity and have enabled at-home nucleic acid testing, as demonstrated during the COVID-19 pandemic, yet their application has so far focused on a limited subset of targets. Similarly, colorimetric and electrochemical enzyme assays for at-home diagnostics are generally applied to high-abundance analytes, such as glucose and lipids[3]. In this context, the ETA platform provides an interfacial potential (Ψ_s) transduction approach using a Ψ_s reporter that generates charged products, thereby modulating Ψ_s of the electrode. This strategy is compatible with biochemical analysis, immunoassays, and molecular diagnostics, while supporting implementation across a broad range of accessibility levels.

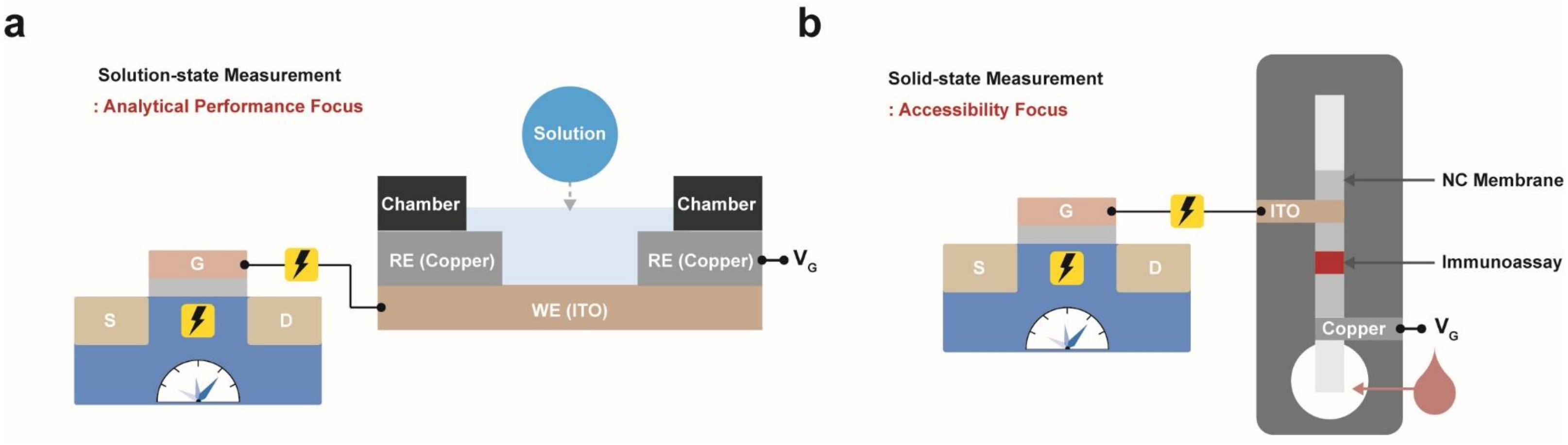

Supplementary Information Fig. 2. Solution-state and solid-state measurements. (a) Solution-state measurement implemented in a well-type format. The indium tin oxide (ITO) WE and copper reference electrode (RE) are directly immersed in a liquid sample within a measurement chamber and electrically coupled to a FET. This format allows direct interaction between reaction products and the electrode interface, supporting high performance biochemical analysis, immunoassays, and molecular diagnostics in this study. (b) Solid-state measurement implemented in a lateral flow immunoassay (LFIA) format for accessibility-oriented operation. The ITO working electrode (WE) and the copper RE are separated by a nitrocellulose (NC) membrane containing the immunoassay region and electrically coupled to a field-effect transistor (FET). Assay reagents are confined within the NC membrane, enabling electrical readout through direct physical contact between the electrode and the NC membrane, thereby supporting portable and simplified workflows.

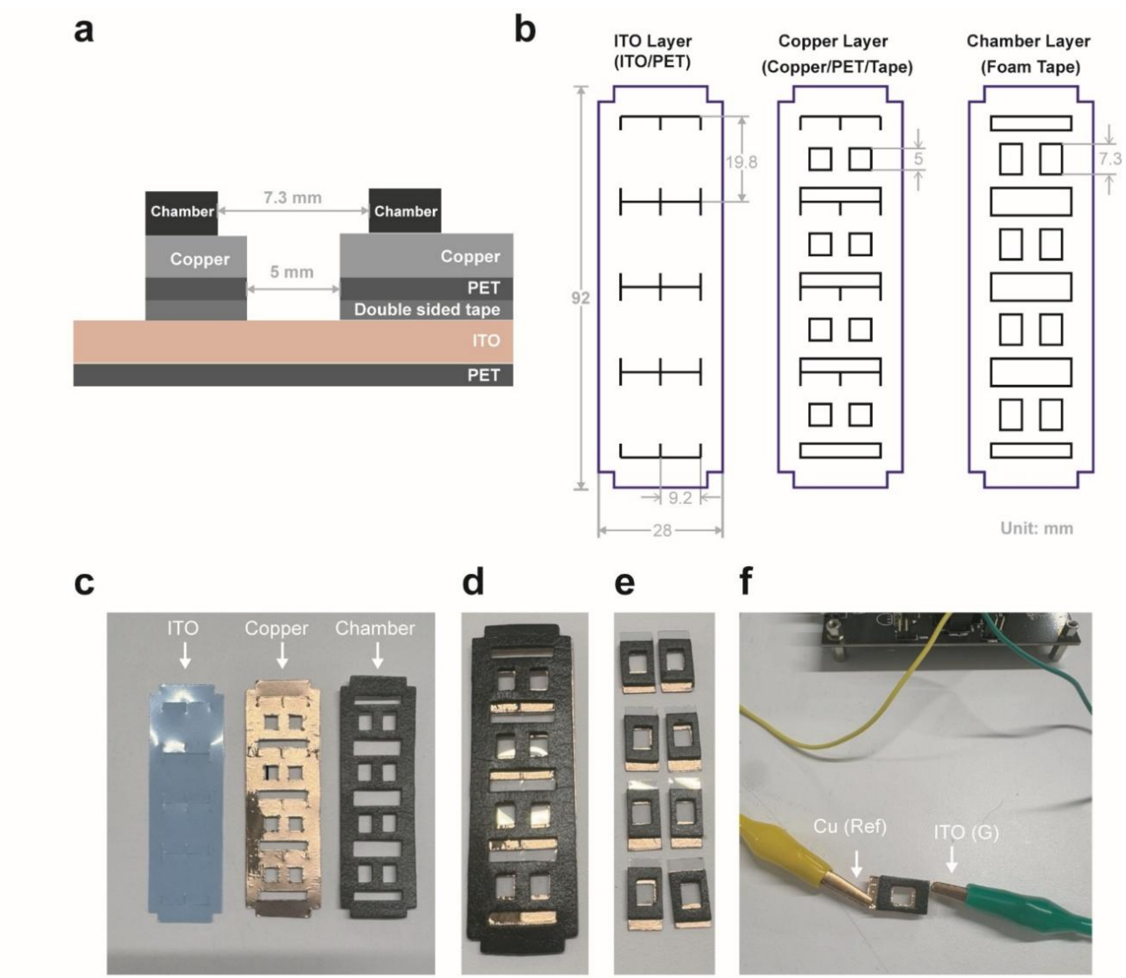

Supplementary Information Fig. 3. Fabrication and configuration of the solution-state ETA electrode assembly. (a) Cross-sectional schematic of a well-type electrode, illustrating the stacked structure comprising a patterned ITO WE on polyethylene terephthalate (PET), a copper RE layer attached above the ITO using double-sided adhesive tape, and a foam-tape chamber defining the reaction volume. (b) Die designs of each layer, including the ITO WE (ITO/PET), the copper (BOMEI, ASIN: B0CLP6C7D4) RE layer (copper/PET/tape), and the chamber layer formed from patterned foam tape. All layers were cut using a die cutter (GrandeMARK 2, AccuCut). (c) Photographs of the fabricated individual layers prior to assembly, showing the patterned ITO layer, copper RE layer, and chamber layer. (d) Photograph of the assembled multilayer electrode stack. (e) Individual well-type electrode units obtained by cutting via a guillotine cutter. (f) Electrical connection of a well-type electrode unit to the FET reader system.

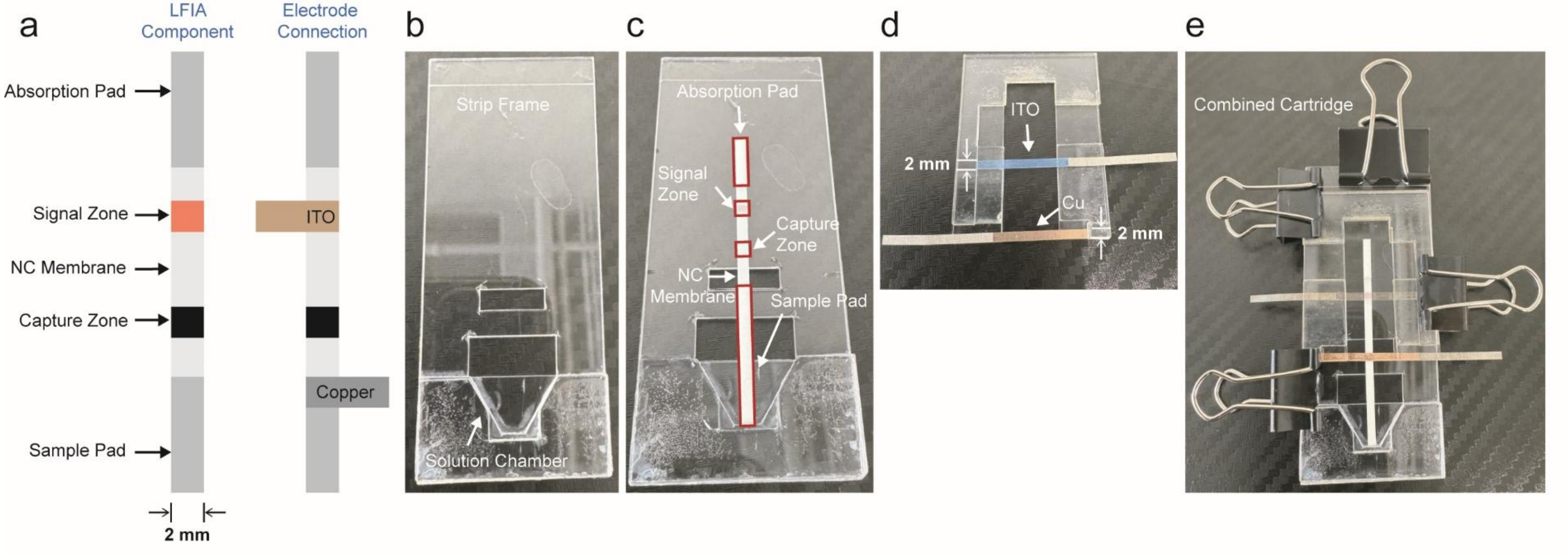

Supplementary Information Fig. 4. Configuration and assembly of the solid-state measurement platform integrated with LFIA. (a) Schematic illustration of the LFIA strip architecture and its electrical interfacing with the electrode assembly. The LFIA strip comprises a sample pad, capture zone and signal zone on a NC membrane, and absorption pad, with a strip width of 2 mm. The signal zone is aligned above the ITO WE, while the copper RE is positioned on top of the sample pad. (b) Photograph of the strip-mounted jig used to accommodate the LFIA strip. (c) Photograph of the LFIA strip placed within the strip-mounted jig, showing the sample pad, NC membrane, capture zone, signal zone, and absorption pad. (d) Photograph of the electrode jig showing the spatially separated ITO WE and copper RE. Coupling of the electrode jig with the strip frame ensures lateral alignment over the designated region of the NC membrane and defines precise vertical spacing to maintain uniform contact pressure. (e) Fully assembled LFIA cartridge, in which the LFIA strip and the electrode jig are integrated and mechanically secured for electrical measurement.

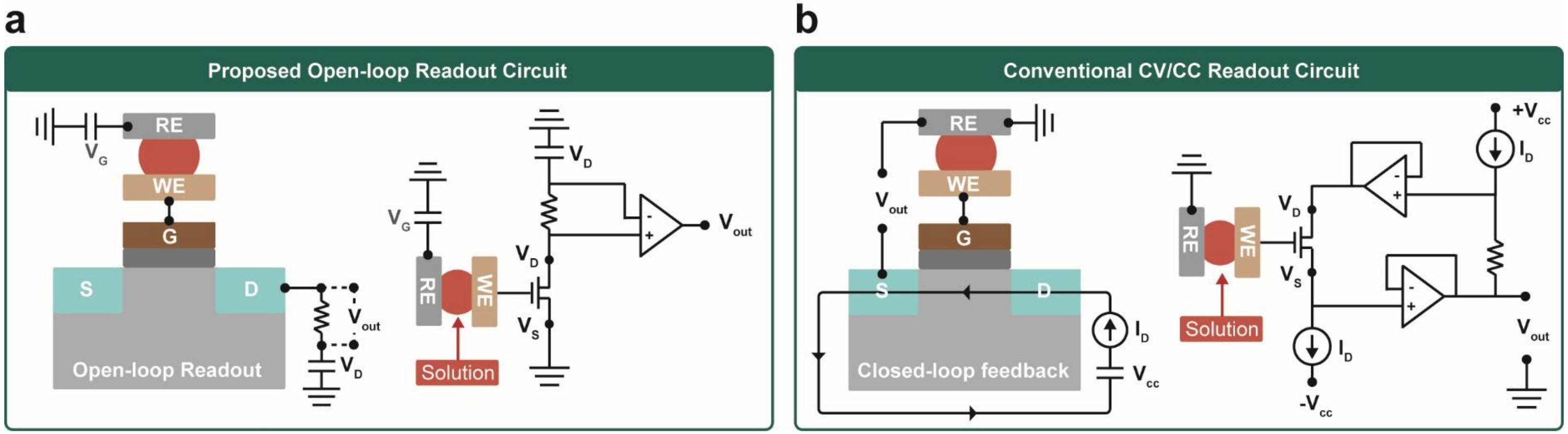

Supplementary Information Fig. 5. Design and implementation of the open-loop readout system for the electrical readout. (a) The proposed open-loop readout circuit for the portable reader eliminates closed-loop feedback[5,6] by directly measuring the drain current (I_D) through a resistor at the drain terminal without potentiostatic control. The measured I_D is subsequently converted into calibrated potential values equivalent to threshold voltage shifts (ΔV_{th}) using the universal calibration method described in the *Standardization of portable FET readout* section. These calibrated values reflect changes in the Ψ_s, enabling device-agnostic scalability across diverse FET-based sensing platforms. (b) Conventional constant-voltage/constant-current (CV/CC) readout circuits [5,6] widely used in electrochemical sensors or conventional FET biosensors operate under closed-loop feedback, maintaining either I_D via continuous reference control. In this way, biological event-induced potential changes are extracted from shifts in gate-source voltage (V_{GS}). Such configurations often require stable silver/silver chloride (Ag/AgCl) REs and continuous feedback, increasing circuit complexity, limiting multiplexing, and making the system vulnerable to drift and hysteresis from electrolyte-free REs.

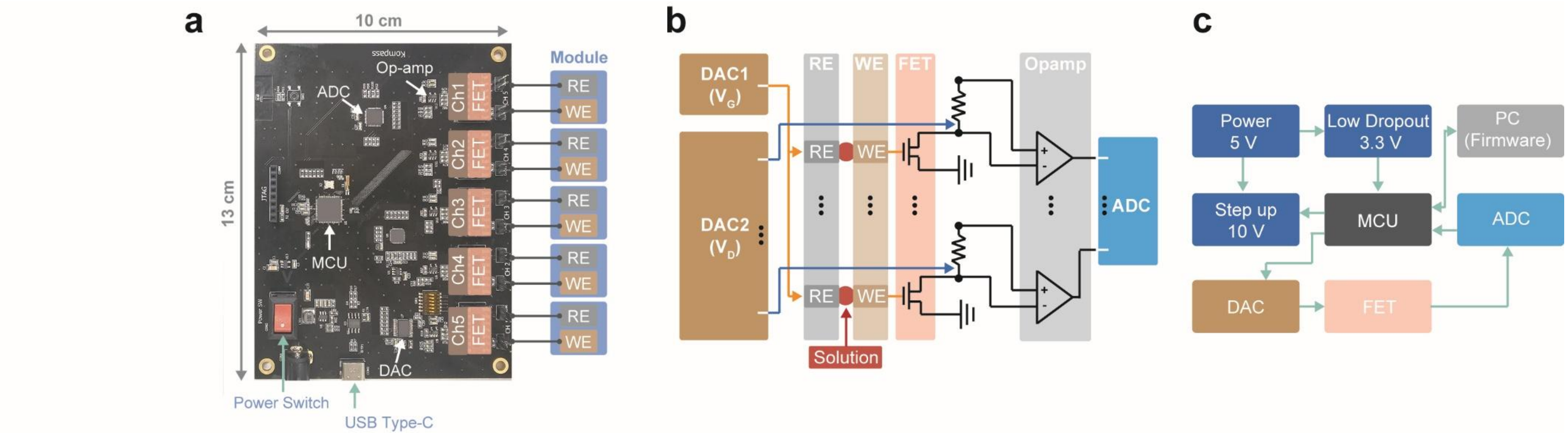

Supplementary Information Fig. 6. Design and architecture of the portable open-loop FET readout system. (a) Photograph of the portable five-channel FET reader (13 × 10 cm) implementing the open-loop architecture. (b) Multiplexed open-loop architecture featuring digital-to-analog converter (DAC)-controlled programmable V_G (fixed or sweeping modes), programmable V_D, current sensing, and op-amp/analog-to-digital convertor (ADC) interfaces. The absence of per-channel feedback loops enables scalable multi-channel integration, allowing independent I_D sensing while sharing a common gate bias. (c) Block diagram of the portable open-loop readout device. A 5 V supply is regulated to 3.3 V and stepped up to 10 V for biasing. Embedded firmware on the reader controls DAC outputs and acquires digitized signals from the ADC, while high-level operation and parameter control are handled by PC software. Processed data are transmitted to the PC for visualization and automated acquisition of transfer characteristics.

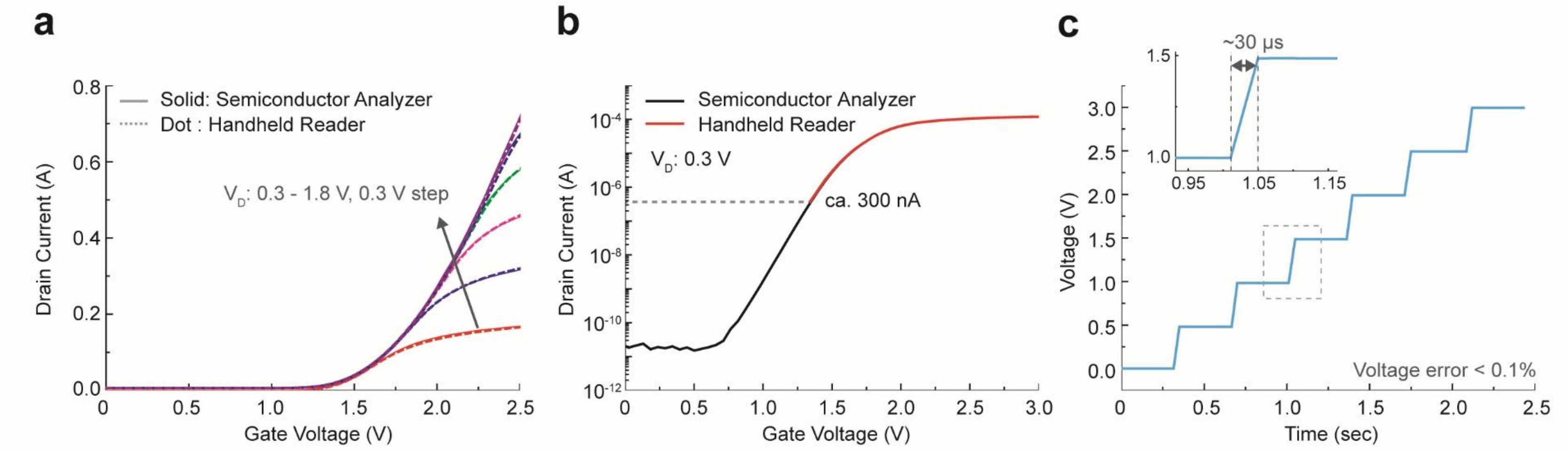

Supplementary Information Fig. 7. Electrical performance of the portable open-loop reader. (a) Intrinsic transfer curves measured without the sensing module show that the portable open-loop reader (dotted) closely matches the characteristics obtained using a semiconductor analyzer (solid) across drain voltages (V_D = 0.3–1.8 V, 0.3 V step). The bias percentage in I_D relative to the semiconductor analyzer remains below 0.05% over the full sweep range. A drain resistance (R_{out}) of 3 kΩ was used for both measurements. (b) Transfer characteristics measured at V_D = 0.3 V using a commercial analyzer (black) and the open-loop reader (red) show consistent behavior, with a minimum detectable drain current of ~300 nA. All characterization in this study is performed in the above-threshold region (I_D >1 μA), ensuring that the detection limit does not affect extraction of transfer curve parameters. (c) Time-resolved DAC output voltage showing stepwise bias-voltage generation over a 0–3.0 V range. The bias voltage is updated at ~30 μs intervals with a voltage error below 0.1%, demonstrating reliable timing control and accurate bias generation for open-loop operation.

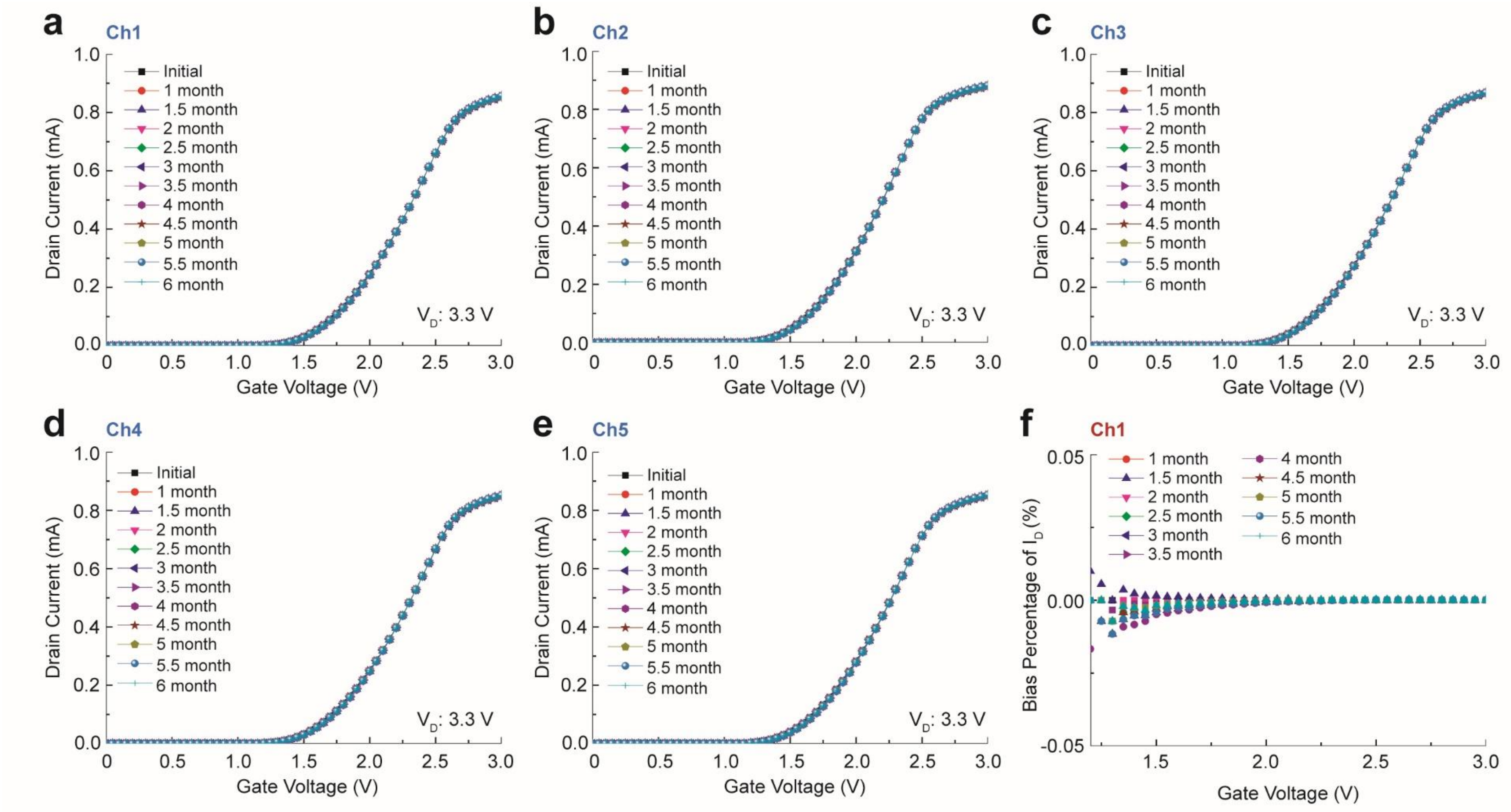

Supplementary Information Fig. 8. Long-term stability of the portable open-loop reader. Transfer curves of a FET assigned to (a) channel 1 (Ch1), (b) Ch2, (c) Ch3, (d) Ch4, and (e) Ch5 of a single open-loop reader, measured over six months at V_D = 3.3 V, demonstrating stable long-term performance of the open-loop reader. (f) Bias percentage of I_D for Ch1 relative to the initial measurement, monitored over the same period, showing negligible drift (<0.05%) across the entire V_G range and confirming that the reader reliably preserves the intrinsic electrical characteristics of the FET over repeated measurements without circuit component degradation.

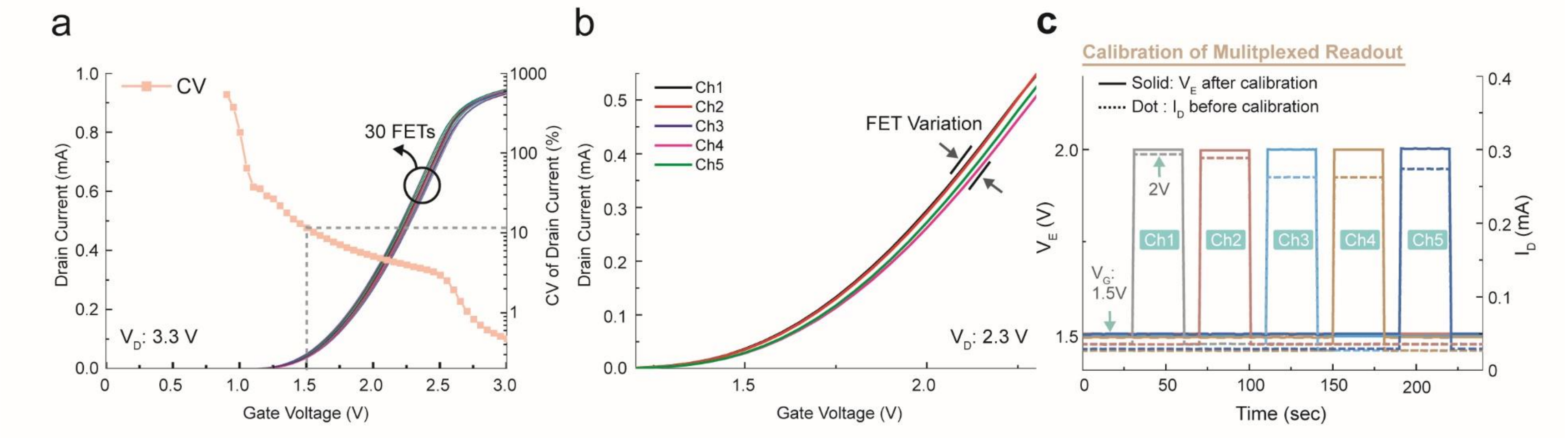

Supplementary Information Fig. 9. Intrinsic FET variation. (a) Transfer curves acquired by the portable open-loop reader from 30 commercial FETs at V_D = 3.3 V. Despite identical device specifications, substantial variation in transfer characteristics is observed, with CV of I_D exceeding 10% near the threshold region (V_{th} ≈ 1.5 V), indicating pronounced intrinsic device-to-device variability. (b) Transfer curves of five different FETs integrated into the portable multiplexed FET reader (Fig. 2a), illustrating channel-to-channel variation arising from inherent differences in FET characteristics. (c) Multiplexed open-loop readout with sequential channel operation. Individual channels are turned on and off in a time-multiplexed manner. The calibrated V_E traces (solid) described in the following section show consistent and independent responses across all five channels, whereas the corresponding raw I_D signals before calibration (dotted) exhibit channel-dependent offsets.

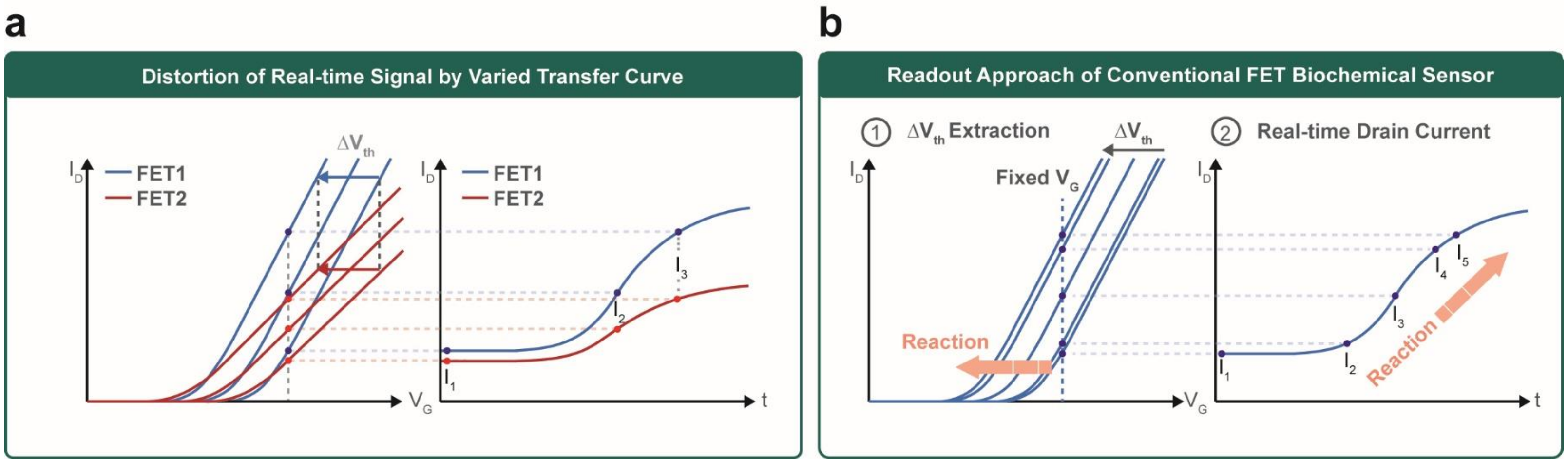

Supplementary Information Fig. 10. Conventional readout approaches in FET biosensors and their limitations. (a) Device-dependent variations by transfer curve characteristics distort real-time I_D signals, as identical biological event-induced $\Delta\Psi_s$ and the corresponding ΔV_{th} can produce inconsistent I_D responses. Although real-time I_D monitoring is simple to implement in a portable readout format, it is highly sensitive to differences in transfer curve shape, leading to inconsistent and device-specific readouts. (b) Two commonly used readout methods in FET biosensors: (1) extraction of ΔV_{th} from repeated transfer curve measurements by sweeping V_G at fixed V_D, and (2) real-time I_D monitoring at fixed V_G and $V_{D.}$ While ΔV_{th} extraction directly quantifies $\Delta\Psi_s$, it requires repeated transfer curve acquisition using bulky semiconductor analyzers, limiting portability.

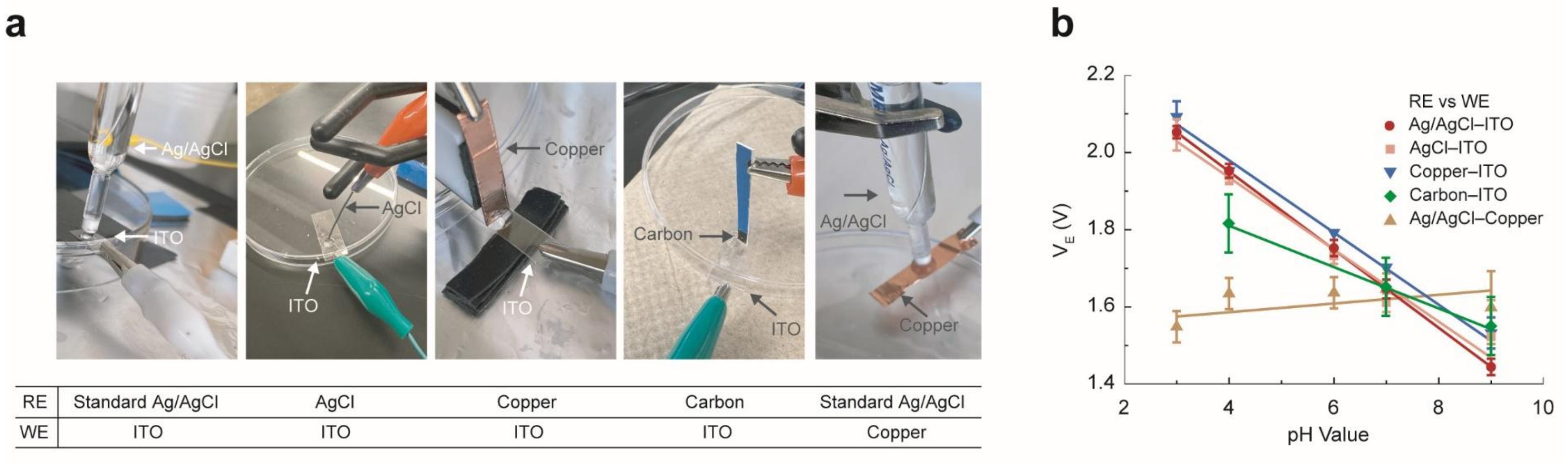

RE	Standard Ag/AgCl	AgCl	Copper	Carbon	Standard Ag/AgCl
WE	ITO	ITO	ITO	ITO	Copper

Supplementary Information Fig. 11. Evaluation of electrode materials as the RE using the open-loop reader. (a) Experimental setup for testing various RE/WE pairs: standard Ag/AgCl–ITO, AgCl–ITO, copper–ITO, carbon–ITO, and Ag/AgCl–copper. Each configuration was evaluated to determine its suitability for stable potential measurement in the ETA system. The pH sensitivities for each configuration were determined to be 50.72, 45.31, 45.35, –3.08, and 20.04 mV/pH, with corresponding r^2 values of 99.99%, 96.34%, 99.07%, 15.6%, and 98.6%, respectively, over the pH range of 3–9. (b) V_E responses as a function of pH for different RE–WE pairings, confirming stable operation of solid-state AgCl and copper REs and showing consistent pH-dependent behavior even with electrolyte-free REs. With a standard Ag/AgCl RE and a copper WE, no linear pH sensitivity was observed, as copper does not exhibit intrinsic pH responsiveness, suggesting that copper behaves as a quasi-reference electrode.

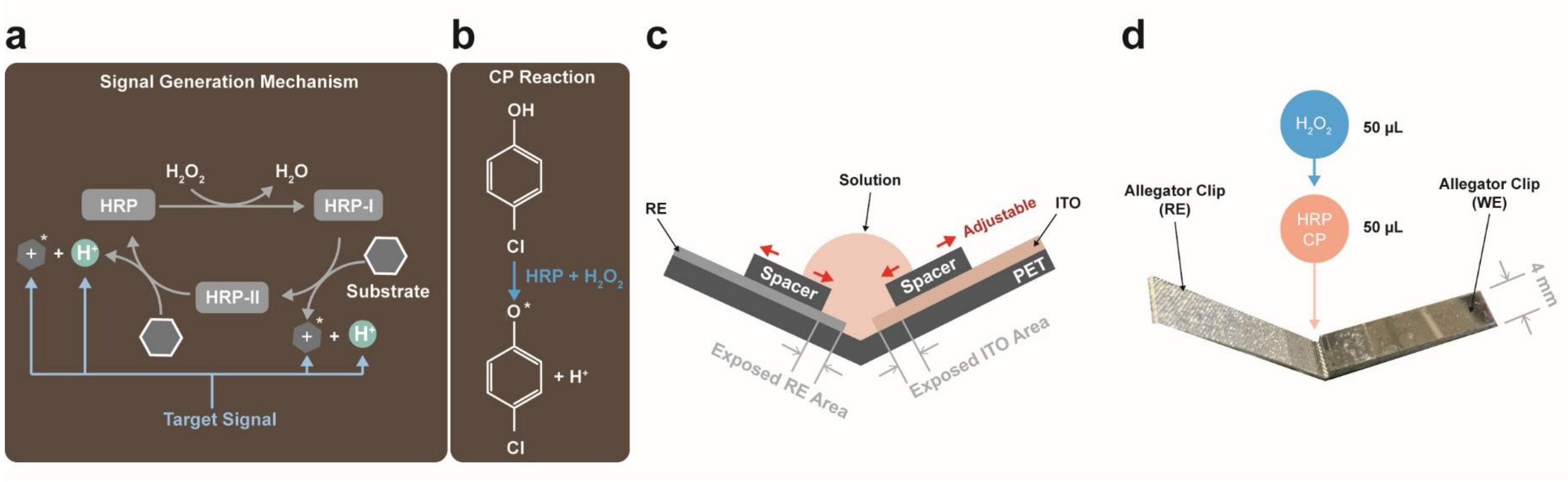

Supplementary Information Fig. 12. Signal-generation mechanism underlying Ψ_s transduction and V-shaped electrode configuration used for evaluation. (a) Schematic illustration of the horseradish peroxidase (HRP) catalytic cycle, showing the formation of reactive HRP intermediates (HRP-I and HRP-II). HRP first reacts with hydrogen peroxide (H_2O_2) to form these intermediates, which subsequently oxidize the substrate, generating protons and charged substrate species that constitute the Ψ_s change of ITO. (b) Reaction scheme of chlorophenol (CP) as a representative HRP substrate, illustrating radical formation and proton generation during HRP–H_2O_2 catalysis. (c) Schematic of the V-shaped electrode, in which laterally adjustable spacers allow controlled variation of the exposed electrode area and spacing between the ITO WE and the RE material. (d) Photograph of the assembled the V-shaped electrode. During measurement, electrical connections between the RE and WE and the open-loop reader were established using alligator clips.

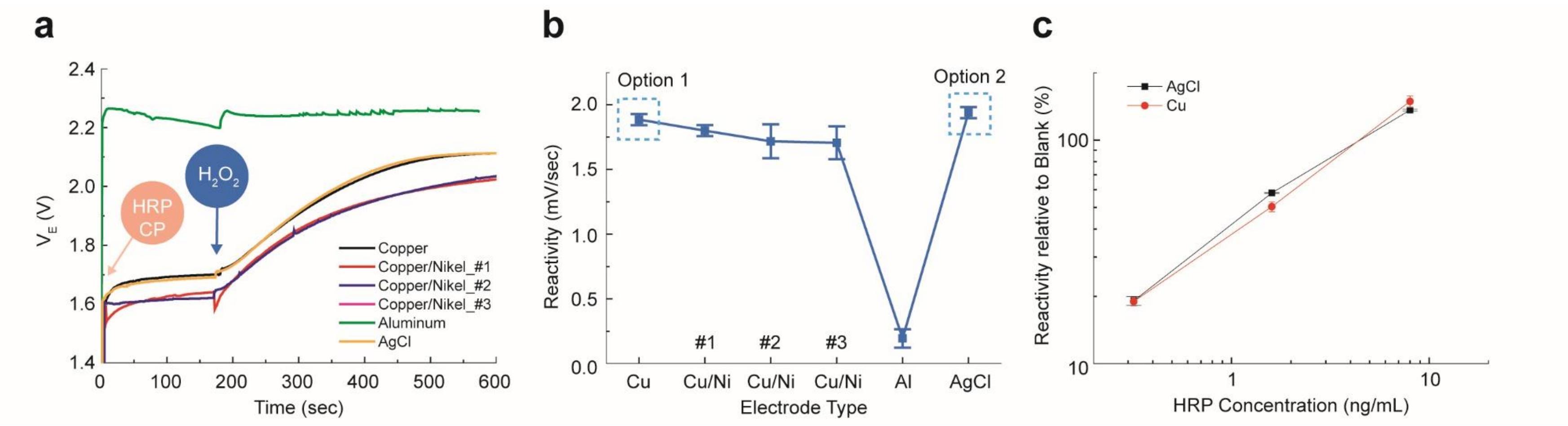

Supplementary Information Fig. 13. Comparative evaluation of electrolyte-free RE materials for solution-state measurement. (a) Representative real-time V_E responses obtained using various RE materials—including copper, three copper–nickel alloy REs sourced from different vendors, aluminum, and printed AgCl—measured under identical HRP–CP–H_2O_2 reaction conditions (10 ng/mL HRP, 3 mM CP, and 1 mM H_2O_2). Copper and AgCl RE exhibited stable baselines and strong Ψ_s shifts, whereas aluminum displayed substantial drift and markedly suppressed signal generation. (b) Reactivity (ΔV_E/sec) calculated for each RE material. Copper and AgCl RE produced the highest reactivity (options 1 and 2), identifying them as optimal RE candidates for stable and high-sensitivity measurements. (c) Reactivity relative to each electrode's no-HRP control (blank), plotted as a function of HRP concentration. AgCl and copper REs exhibit nearly identical quantitative responses across the tested HRP concentration range, confirming their interchangeability for solution-state measurements.

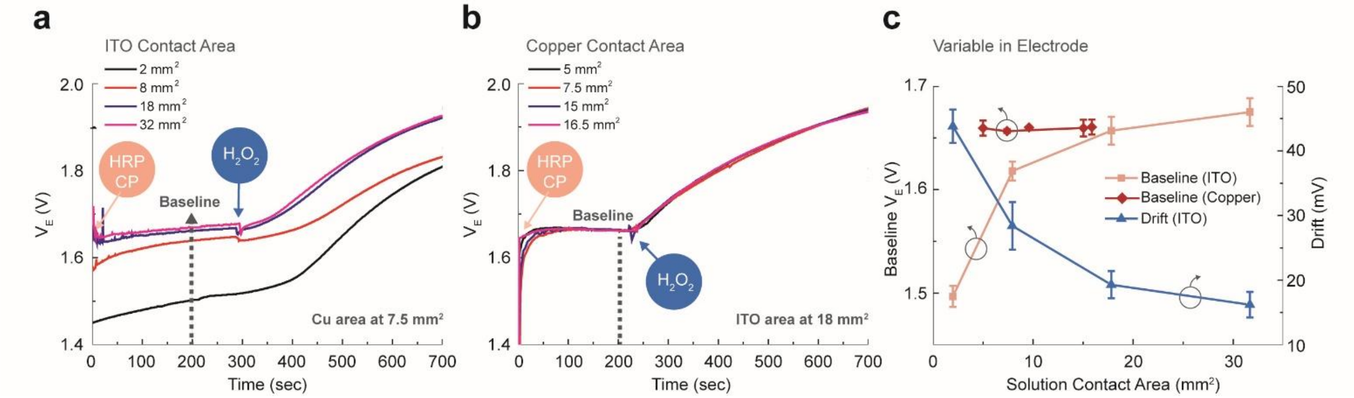

Supplementary Information Fig. 14. Electrode dimension optimization for solution-state measurement. (a) Representative V_E curves for HRP–CP–H_2O_2 reactions (5 ng/mL HRP, 3 mM CP, and 1 mM H_2O_2) measured on ITO WE with different contact areas (2–32 mm²), showing that baseline V_E level and signal magnitude increase and begin to saturate when the ITO contact area exceeds ~18 mm². (b) Representative V_E curves obtained using copper REs with varying contact areas (5–16.5 mm²), illustrating that the copper RE area does not affect baseline stability or drift during the reaction. (c) Summary of baseline V_E level and drift as a function of electrode contact area, demonstrating that baseline stabilization is achieved and drift becomes negligible once the ITO contact area exceeds ~18 mm².

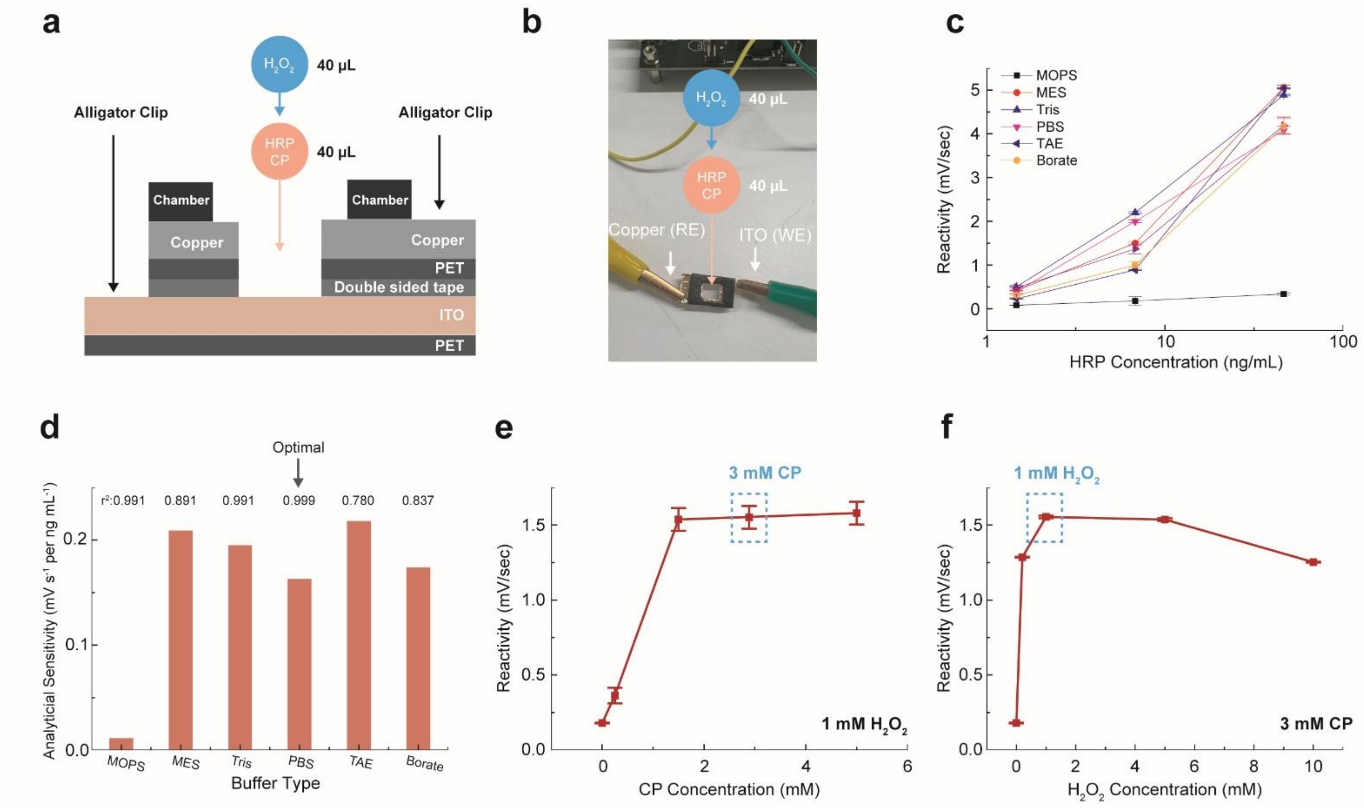

Supplementary Information Fig. 15. Optimization of standard measurement conditions for solution-state assays. (a) Schematic illustration of the well-type electrode used for solution-state measurements. (b) Measurement protocol for the HRP reaction. An initial 40 µL of HRP and CP solution is added to the well-type electrode, followed by injection of 40 µL of H_2O_2 to initiate the reaction. (c) Reactivity as a function of HRP concentration measured in different buffer systems—3-(N-morpholino)propanesulfonic acid (MOPS), 2-(N-morpholino)ethanesulfonic acid (MES), Tris(hydroxymethyl)aminomethane (Tris), phosphate-buffered saline (PBS), Tris–acetate–EDTA (TAE), and borate buffer—under identical reaction conditions (3 mM CP and 1 mM H_2O_2). All buffers exhibit comparable kinetic responses except acidic MOPS, which yields a substantially reduced signal. (d) Analytical sensitivity extracted from the slopes in (c) for each buffer system. Comparable performance was observed across most buffers, with PBS exhibiting the highest linearity ($r^2 = 0.999$) across HRP concentrations and therefore selected as the standard buffer for subsequent experiments. Outside acidic conditions, analytical sensitivity of HRP remained largely consistent; however, linearity was affected, influencing reactivity at low HRP concentrations. (e) Reactivity as a function of CP concentration (0–5 mM) measured with 8 ng/mL HRP and 1 mM H_2O_2, showing saturation near 3 mM CP. (f) Reactivity as a function of H_2O_2 concentration (0–10 mM) measured with 8 ng/mL HRP and 3 mM CP, revealing an optimal response at approximately 1 mM H_2O_2.

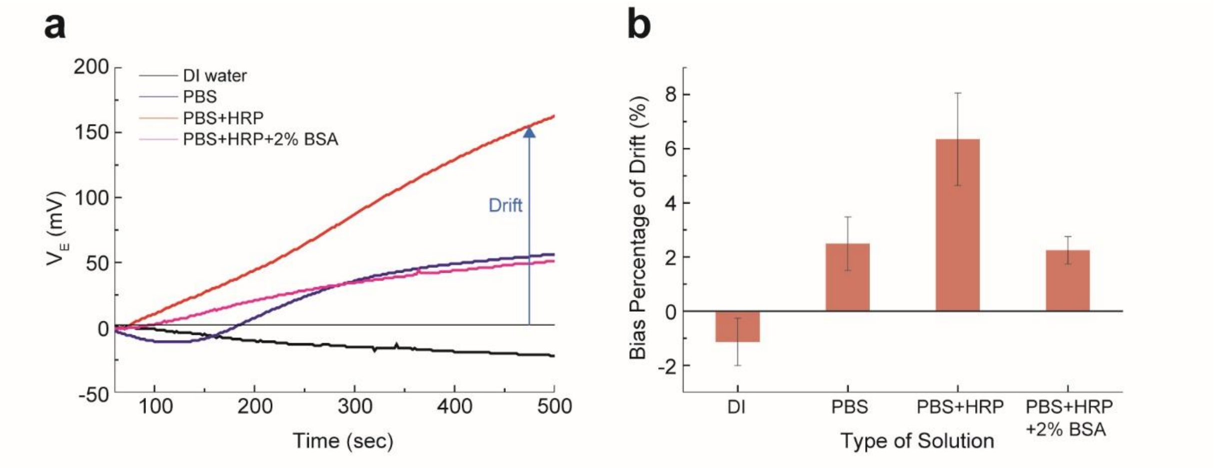

Supplementary Information Fig. 16. Drift behavior under different testing buffer conditions in well-type electrode. (a) V_E drift traces measured in DI water, PBS, PBS containing HRP, and PBS containing HRP with 2% BSA. A pronounced drift is observed in PBS + HRP, likely arising from nonspecific adsorption of HRP onto the ITO surface. Addition of 2% BSA substantially suppresses this drift by providing an effective blocking layer on the electrode surface. (b) Bias percentage of drift under each condition, calculated by comparing V_E at 500 sec to the initial V_E. Minimal drift was observed in DI water and PBS, whereas markedly increased drift occurred in PBS + HRP, likely due to surface adsorption. Addition of 2% BSA substantially suppressed the drift.

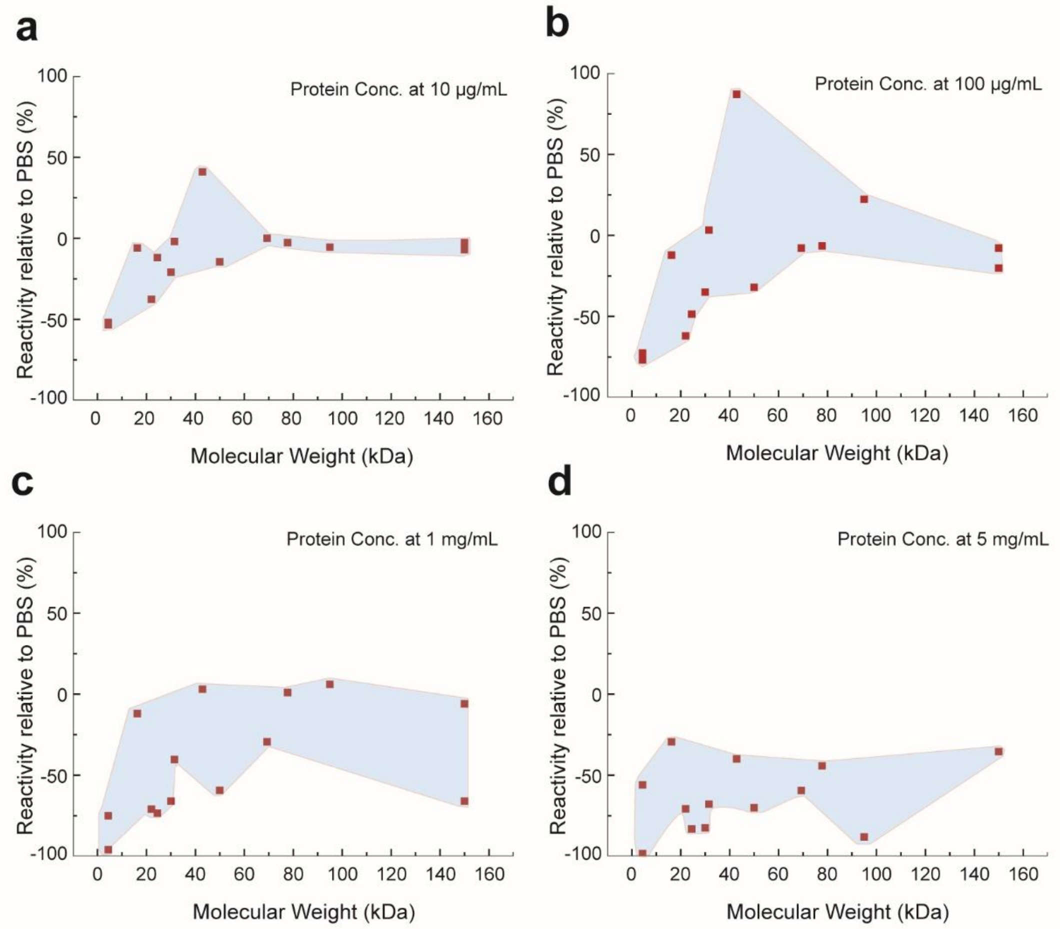

Supplementary Information Fig. 17. Influence of protein MW on reactivity across protein concentrations. Reactivity relative to the no-protein PBS control plotted as a function of protein MW for the proteins tested in Extended Data Fig. 5 at four concentrations: (a) 10 µg/mL, (b) 100 µg/mL, (c) 1 mg/mL, and (d) 5 mg/mL. At low protein concentrations (10–100 µg/mL), reactivity shows a noticeable MW-dependent tendency, where lower-MW proteins generally induce stronger suppression or modulation of the HRP signal, suggesting that smaller proteins more effectively interact with or block the electrode interface. At higher concentrations (1–5 mg/mL), this MW-related tendency becomes less distinct, and reactivity is broadly suppressed across all protein sizes, consistent with surface saturation and loss of size-dependent effects.

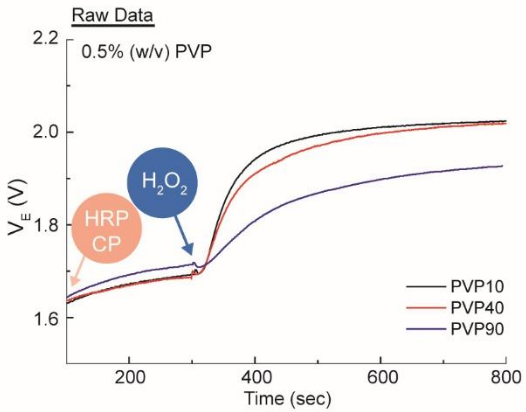

Supplementary Information Fig. 18. MW–dependent effects of polyvinylpyrrolidone (PVP) on reactivity under controlled conditions. Real-time V_E traces measured with 0.5% (w/v) PVP of different molecular weights, showing that higher-MW leads to greater electrical signal suppression.

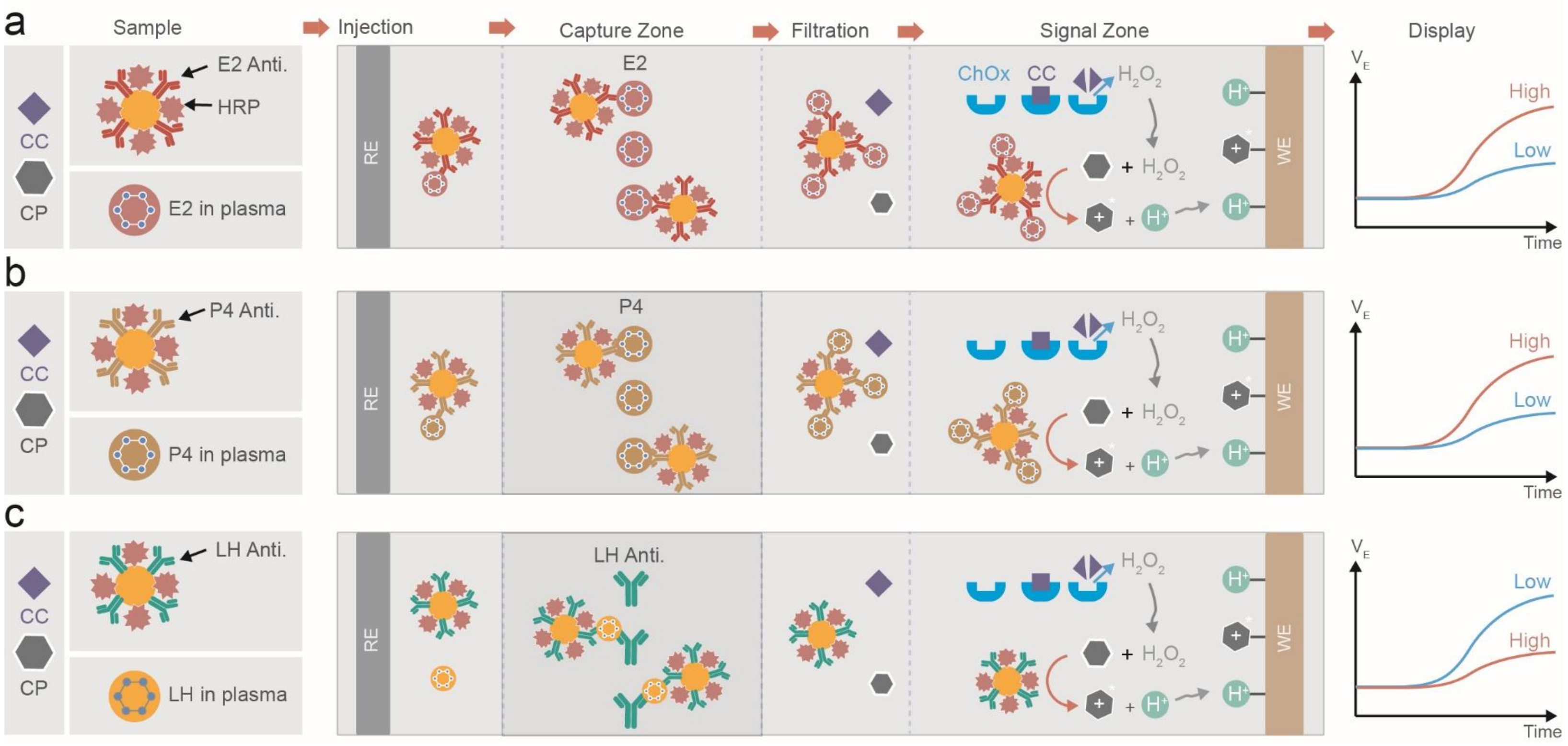

Supplementary Information Fig. 19. Operational mechanisms of ETA-integrated LFIA system for hormone detection. (a) Schematic illustration of the ETA-integrated competitive LFIA for estradiol (E2) detection. The sample contains E2, anti-E2 antibody-HRP–gold nanoparticle (AuNP) conjugate, CC, and CP substrate, which migrate along the NC membrane. In the capture zone, E2 antigen is immobilized, enabling competitive binding between E2 and the conjugate. When E2 is high, fewer conjugates bind in the capture zone and instead pass toward the signal zone. There, ChOx converts CC into H_2O_2, enabling HRP to generate charged products, which produce the Ψ_s shift detected at the ITO gate. As a result, higher E2 concentrations yield higher electrical signals, characteristic of the competitive assay format. (b) The same competitive LFIA workflow as in panel (a), configured for progesterone (P4) detection. (c) Schematic illustration of the ETA-integrated sandwich LFIA for luteinizing hormone (LH) detection. The sample contains LH and the anti-LH detection antibody-HRP–AuNP conjugate, which migrate along the NC membrane. In the capture zone, immobilized anti-LH capture antibodies bind LH, forming the first layer of the sandwich complex. The conjugate then binds to the captured LH, completing the sandwich structure. When LH concentration is high, more conjugate is retained in the capture zone, and fewer conjugates reach the signal zone. Consequently, higher LH concentrations yield lower electrical signals.

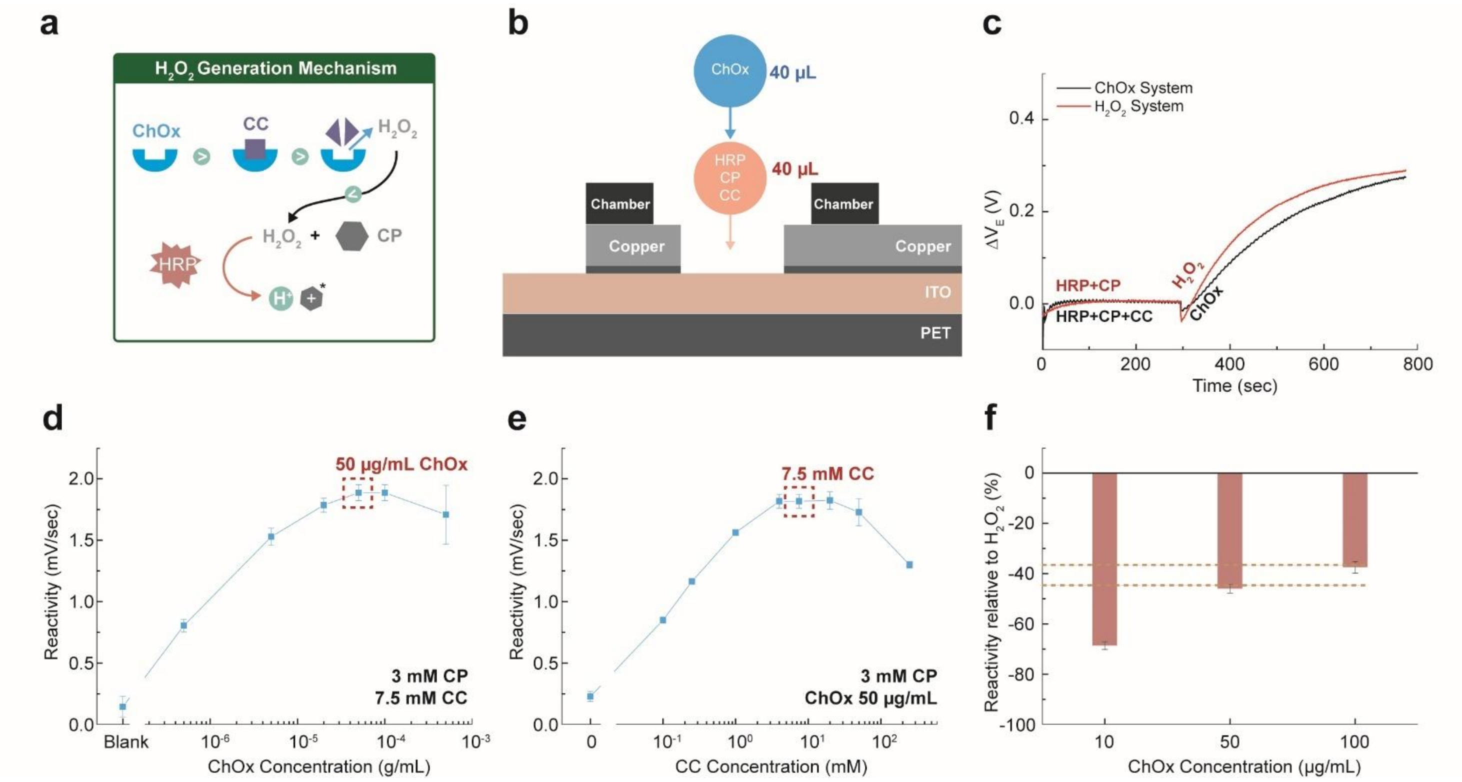

Supplementary Information Fig. 20. In situ H_2O_2 generation using ChOx for solution-state measurement. (a) Schematic of the ChOx-mediated H_2O_2 generation pathway, where ChOx oxidizes CC to produce H_2O_2, which subsequently drives the HRP–CP reaction to generate protons and charged intermediates responsible for the electrical signal. (b) Schematic illustration in the experimental setup for the ChOx-based in situ H_2O_2 generation system, where 40 μL of HRP/CP/CC solution is added onto the well-type electrode, followed by the addition of 40 μL of ChOx solution to initiate H_2O_2 generation. (c) Representative real-time ΔV_E traces comparing the ChOx–CC system with direct H_2O_2 addition under identical HRP and CP conditions, showing that ChOx-generated H_2O_2 produces a reduced reactivity. (d) Reactivity as a function of ChOx concentration measured at 20 ng/mL HRP, 3 mM CP, and 7.5 mM CC, identifying ~50 μg/mL ChOx as the optimal enzyme concentration. (e) Reactivity as a function of CC concentration measured at 20 ng/mL HRP, 3 mM CP, and 50 μg/mL ChOx, identifying ~7.5 mM CC as the optimal substrate concentration. (f) Reactivity by the ChOx-mediated H_2O_2 generation expressed relative to the direct H_2O_2 system across different ChOx concentrations, showing saturation above ~50 μg/mL ChOx, indicating stable in situ H_2O_2 generation without further signal enhancement at higher enzyme levels. Overall, the ChOx-mediated route yields an approximately 40% lower reactivity compared to direct H_2O_2 addition, while still providing stable and reproducible in situ H_2O_2 generation.

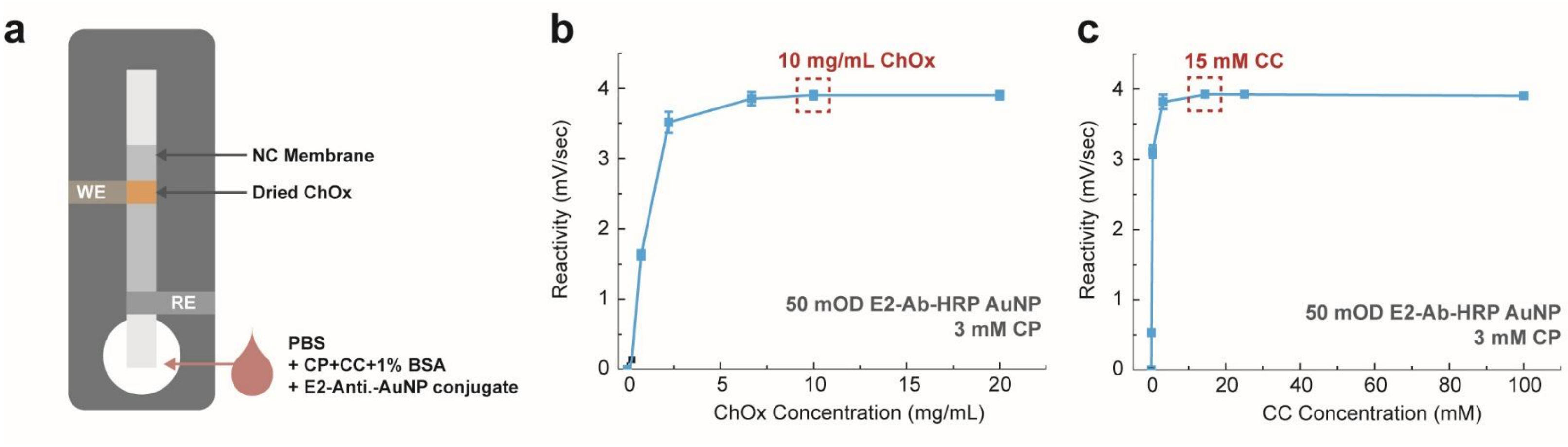

Supplementary Information Fig. 21. Solid-state measurement incorporated with in situ H_2O_2 generation. (a) Schematic illustration of the LFIA system incorporating a dried ChOx region at a designated location, with the ITO WE positioned directly above the ChOx zone. This cartridge does not include an immunoassay function and contains dried ChOx only. During lateral flow, CC and HRP/CP reagents migrate to the dried ChOx region beneath the ITO electrode, enabling in situ H_2O_2 generation without direct H_2O_2 addition. (b) Reactivity as a function of ChOx concentration in the LFIA format, measured at 50 mOD E2–antibody–HRP AuNP conjugates and 3 mM CP, showing rapid saturation and identifying ~1 mg/mL ChOx as sufficient for stable signal generation. (c) Reactivity as a function of CC concentration measured at 50 mOD E2–antibody–HRP AuNP conjugates and 3 mM CP, exhibiting saturation at ~15 mM CC under solid-state measurement.

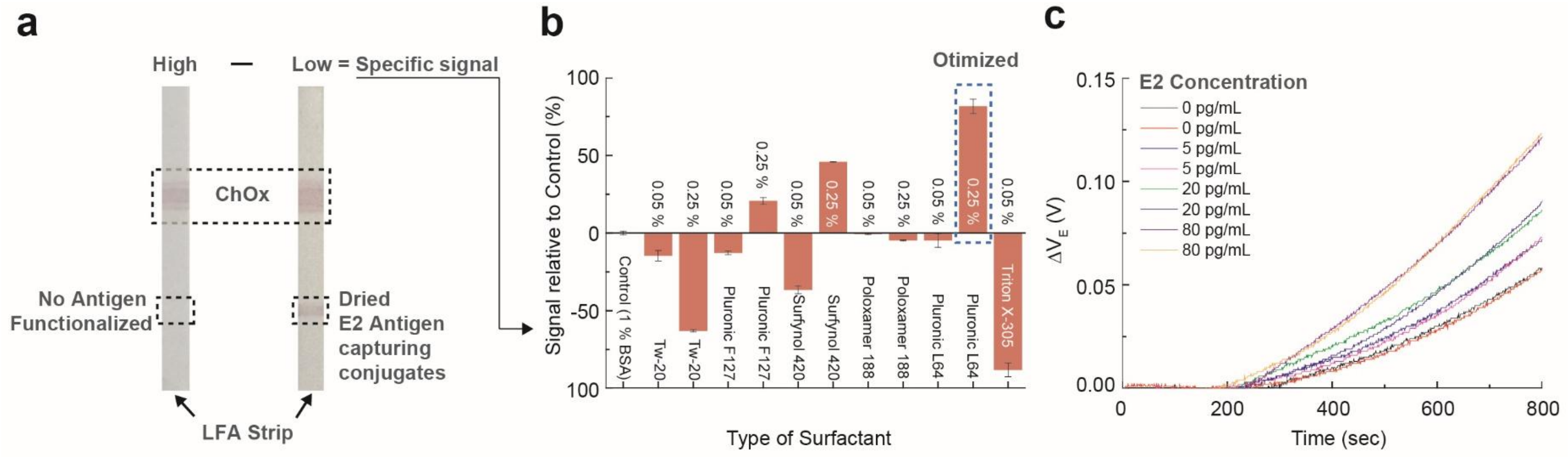

Supplementary Information Fig. 22. Optimization of assay components for solid-state measurement. (a) Photograph of two LFIA strips used for platform optimization. Both strips contain a dried ChOx region located on the upper side of the LFIA strip, upstream of the signal zone. In one strip (right), E2 antigen is dried in the capture zone, whereas the other strip (left) contains no immobilized antigen. In the antigen-functionalized strip on the right, immobilized E2 captures the 50 mOD E2–antibody–HRP AuNP conjugates during lateral flow, producing a visible pink band and reducing the amount of conjugate reaching the signal zone, which results in a lower electrical signal. In contrast, the antigen-free strip shows no visible capture, allowing the antibody–conjugate to fully reach the signal zone and generate the maximum signal. The difference in signal response between the antigen-free and antigen-functionalized strips represents the specific immunoassay signal. (b) Surfactant screening for the LFIA format. Signal changes are shown relative to the control condition consisting of 1% BSA with no surfactant. Among the tested surfactants and concentrations, Pluronic L64 at 0.25% (w/v) yields the highest signal response and was selected for subsequent solid-state measurements. (c) Representative real-time ΔV_E traces measured over a range of spiked E2 concentrations (0, 5, 20, and 80 pg/mL) from duplicate LFIA measurements under the optimized surfactant condition identified in panel (b). Spiked E2 in the optimized running buffer was used to evaluate the assay performance. The traces show high uniformity across measurements and clear distinction among different concentrations.

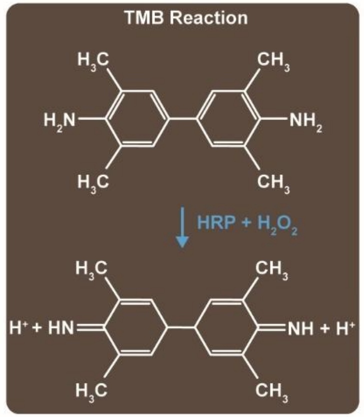

Supplementary Information Fig. 23. TMB-based Ψ_s transduction. Reaction scheme of the HRP–H_2O_2–TMB signaling system, where HRP-catalyzed oxidation of TMB generates protons that contribute to the electrical signal at the ITO interface.

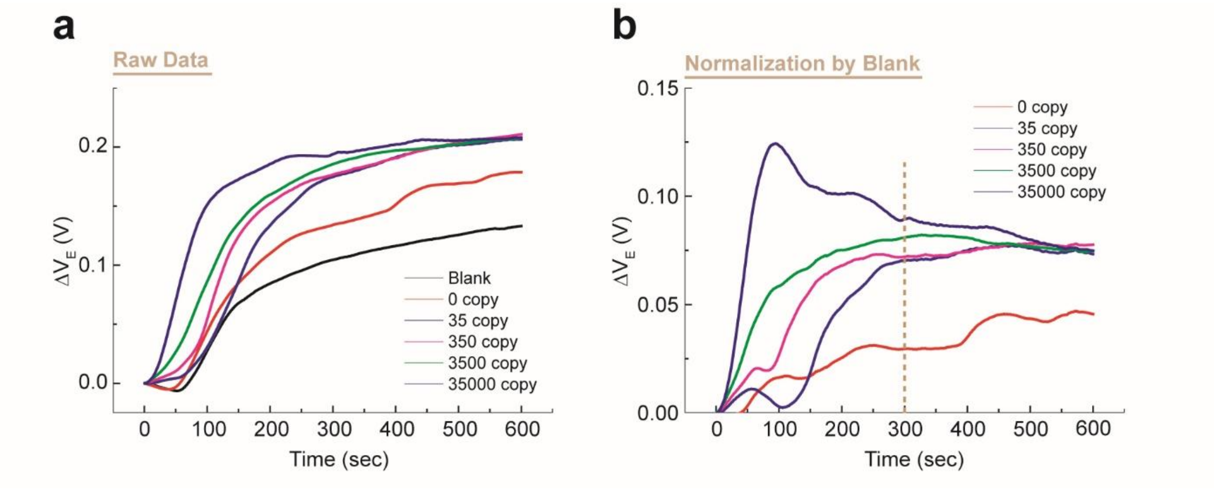

Supplementary Information Fig. 24. Raw and normalized electrical responses in LAMP. (a) Raw real-time ΔV_E traces, baseline-normalized to 0 V, obtained at different HBV DNA copy numbers (0, 35, 350, 3500, and 35000 copies). (b) The same ΔV_E traces after normalization to the blank condition (no $MgSO_4$), revealing clear copy-number-dependent separation of LAMP amplification kinetics within 5 min.

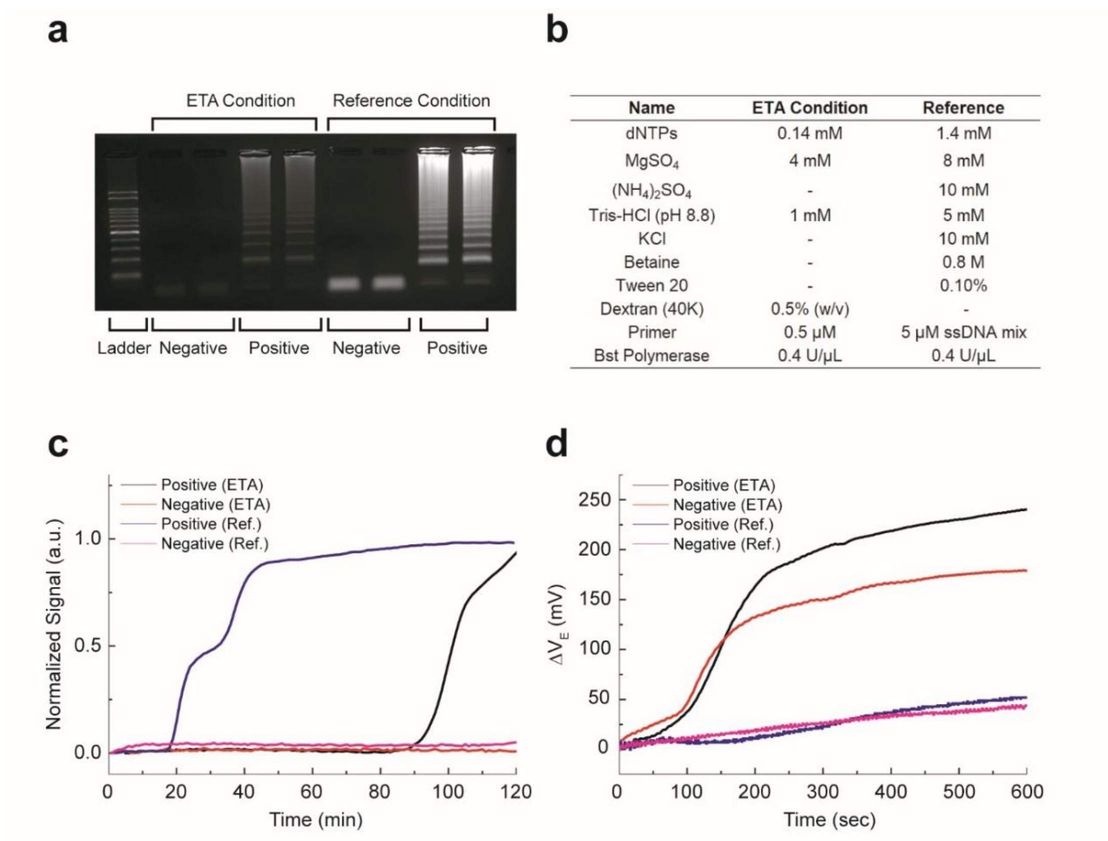

Name	ETA Condition	Reference
dNTPs	0.14 mM	1.4 mM
$MgSO_4$	4 mM	8 mM
$(NH_4)_2SO_4$	-	10 mM
Tris-HCl (pH 8.8)	1 mM	5 mM
KCl	-	10 mM
Betaine	-	0.8 M
Tween 20	-	0.10%
Dextran (40K)	0.5% (w/v)	-
Primer	0.5 μM	5 μM ssDNA mix
Bst Polymerase	0.4 U/μL	0.4 U/μL

Supplementary Information Fig. 25. Experimental evidence validating LAMP in electrical readout. (a) Agarose gel electrophoresis of LAMP products after 120 min incubation, comparing reactions performed under (b) the optimized condition for electrical readout and a conventional fluorescence-optimized reference condition. Positive samples contained 35000 copies of HBV DNA, whereas negative controls were incubated without $MgSO_4$. Clear amplification bands are observed under both conditions, confirming successful DNA amplification using the optimized formulation for electrical readout. Reaction compositions are listed, highlighting reformulation for electrical readout rather than fluorescence optimization. (c) Time-resolved fluorescence signals measured using EvaGreen under the reference and optimized conditions for electrical readout. While the reference condition produces detectable fluorescence <20 min, the ETA-optimized condition requires >80 min for the signal to exceed the threshold, indicating that the ETA formulation is not optimized for fluorescence-based detection. (d) Real-time electrical readout of the same LAMP reactions shows rapid and distinct ΔV_E separation between positive and negative samples within 5 min, whereas the reference condition optimized for optical analysis does not exhibit a distinguishable signal due to interference from individual reaction components under the electrical measurement scheme.

Supplementary Information Table 1. Comparative performance of ETA across biochemical, immunoassay, and molecular diagnostic modalities. Comparisons were primarily based on commercially available diagnostic products to ensure clinically relevant benchmarking. In cases where no established commercial product was available for a given analyte or format, representative peer-reviewed literature reports were included. Abbott i-STAT was incorporated as a reference electrochemical platform owing to its broad clinical adoption and commercial success. Entries for high-sensitivity Troponin I (hs-TnI) and total beta human chorionic gonadotropin (β-hCG) are provided for contextual comparison. ECLIA and qPCR denote electrochemiluminescence immunoassay and quantitative PCR, respectively.

Modality	Biomarker	Type	Transduction /Format	Matrix (Sample type)	Accessibility*	LOD	Time	Reference
Biochemical	**Glucose**	Optical	Colorimetry/Electrode strip	Blood	3	10 mg/dL	5 sec	Roche Accu-Chek
		Electrochemical	Redox/Electrode strip	Blood	3	20 mg/dL	5 sec	Abbott Freestyle
		ETA	**Ψ_s/Well-type**	**Buffer (spiked)**	**3**	**0.92 µg/dL**	<20 sec	**This work**
Immunoassay	**E2**	Optical	Colorimetry/LFIA	Serum/plasma	3	15 pg/mL	10 min	Vitrosens
			Fluorescence/LFIA	Serum/plasma	2	9–30 pg/mL	23 min	Wanfo
			ECLIA/Well-type	plasma/serum	1	5 pg/mL	18 min	Roche Elecsys
		Electrochemical	Redox/Voltammetry	Serum	N/A	5.4 pg/mL	70 min	[8]
		ETA	**Ψ_s/LFIA**	**Plasma**	**3**	**0.146 pg/mL**	**10 min**	**[9]**
	P4	Optical	Colorimetry/LFIA	Serum/plasma	3	0.35 ng/mL	10 min	Vitrosens
			Fluorescence/LFIA	Serum/plasma	2	0.157 ng/mL	23 min	Wanfo
			ECLIA/Well-type	Serum/plasma	1	50 pg/mL	18 min	Roche Elecsys
		Electrochemical	Redox/Voltammetry	Bovine Serum	N/A	80 pg/mL	40 min	[10]
		ETA	**Ψ_s/LFIA**	**Plasma**	**3**	**0.089 ng/mL**	**10 min**	**This work**
	LH	Optical	Colorimetry/LFIA	Serum/plasma	3	10–25 mIU/mL	15 min	Vitrosens
			Fluorescence/LFIA	Blood/plasma/serum	2	0.1 mIU/mL	15 min	Wanfo
			ECLIA/Well-type	Serum/plasma	1	0.10 mIU/mL	18 min	Roche Elecsys
		Electrochemical	Redox/Voltammetry	Serum	N/A	1.9 mIU/mL	50 sec	[11]
		ETA	**Ψ_s/LFIA**	**Plasma**	**3**	**0.045 mIU/mL**	**10 min**	**This work**
	HIV-1 p24	Optical	Colorimetry/LFIA	Blood/plasma/serum	4	N/A	20 min	Abbott Determine
			Fluorescence/Well-type	Serum	N/A	200 fg/mL	7.5 min	[12]
		Electrochemical	Redox/Voltammetry	Buffer (spiked)	N/A	83 fg/mL	N/A	[13]
		ETA	**Ψ_s/IMS+Well-type**	**Buffer (spiked)**	**3**	**44.8 fg/mL**	**20 min**	**This work**
Molecular diagnostic	**HBV DNA**	Optical	Fluorescence/qPCR	Serum/plasma	1	20–40 copies/mL	<3.5 h	Roche Cobas
			Colorimetry/LAMP	Plasma	N/A	10000 copies/ mL	45 min	[14]
		ETA	**Ψ_s/LAMP+Well-type**	**Purified DNA**	**3**	**<35 copies/test**	**<5 min**	**This work**
Immunoassay	**hs-TnI**	Electrochemical	Redox/Amperometry	Blood/plasma	3	2.9 pg/mL	>15 min	Abbott i-STAT
	Total β-hCG				3	5 mIU/mL	10 min	Abbott i-STAT

*Accessibility was graded based on readout requirements as follows: **4**, no bulky instrumentation required (visual or disposable readout); **3**, portable reader required; **2**, benchtop analyzer required; **1**, centralized laboratory system.

Supplementary Information Table 2. Materials used for matrix-interference and formulation screening. Proteins, ionic species, sugars, and polymers evaluated in this study, including vendor information, catalog numbers, MW, pI, and test concentrations. Protein pI and MW values were obtained from vendor-provided specifications, with approximate values indicated where applicable. Ionic species were tested at a fixed concentration unless otherwise noted. Sugars and polymers were evaluated at identical weight fractions to assess formulation-dependent modulation of Ψ_s.

Category	Component	Vendor	Catalog No.	MW (kDa)	pI value	Test concentration
Proteins	BSA	Thermo Scientific	37525	~69	5.6	0–50 mg/mL
	Ovalbumin	Sigma-Aldrich	S7951	~42	4.5	0–20 mg/mL
	Casein (Blocker)	Thermo Fisher	37528	~24	4.9	0–5 mg/mL
	Choline oxidase	Toyobo	CHO-301	~95	4.1	0–5 mg/mL
	Peptide Fragment	Toyobo	BPF-301	~22		0–10 mg/mL
	Protamine	Sigma-Aldrich	P4005	~4.3	13.3	0–5 mg/mL
	Mouse IgG	SouthernBiotech	0107-01	~150	7	0–1.25 mg/mL
	Lysozyme	Sigma-Aldrich	L6876	~16	9.36	0–10 mg/mL
	Neo Protein Saver	Toyobo	NPS-301	~30		0–10 mg/mL
	γ-Globulins	Sigma-Aldrich	G5009	~150	7	0–10 mg/mL
	holo-transferrin	Sigma-Aldrich	T1283	~77	5.8	0–5 mg/mL
	Protamine sulfate	Sigma-Aldrich	P4020	~4.3	13.3	0–25 mg/mL
	Concanavalin A	Sigma-Aldrich	L7647	~31	5.5	0–5 mg/mL
	Soy acid hydrolysate	Sigma-Aldrich	S1674			0–50 mg/mL
	Gelatin	Sigma-Aldrich	G2625	~50		0–25 mg/mL
Ionic and others	NaCl	Sigma-Aldrich	S9888			5 mM
	$(NH_4)_2SO_4$	Sigma-Aldrich	A4915			
	$MgCl_2$	Sigma-Aldrich	M8266			
	$MgSO_4$	Sigma-Aldrich	208094			
	$MnSO_4$	Sigma-Aldrich	M7634			
	$CuCl_2$	Sigma-Aldrich	459097			
	$FeSO_4$	Sigma-Aldrich	F8633			
	L-Lysine	Sigma-Aldrich	L5501	~0.15		0.5% (w/v)
	Heparin	Sigma-Aldrich	H3393	~15		
	AuNP (15 nm)	Ted Pella	15704-1			1 OD
Sugers & Polymers	Trehalose	Sigma-Aldrich	T5251	~0.34		0.5% (w/v)
	Sucrose	Sigma-Aldrich	S0389	~0.34		
	Dextran	Sigma-Aldrich	D1662	~70		
	Dextran sulfate	Sigma-Aldrich	31404	~5		
	Dextran sulfate	Thermo Fisher	J63606	~40		
	Dextran sulfate	Sigma-Aldrich	D8906	~500		
	Polyvinylpyrrolidone	Sigma-Aldrich	PVP10	~10		
	Polyvinylpyrrolidone	Sigma-Aldrich	PVP40	~40		
	Polyvinylpyrrolidone	Sigma-Aldrich	PVP90	~90		
	Polyethylene glycol	Sigma-Aldrich	202371	~0.3		
	Polyethylene glycol	Sigma-Aldrich	86101	~1.5		

Supplementary Information Table 3. List of surfactants screened in this study.

Name	Class	Vendor	Catalog No.	MW (g/mol)	HLB
Aerosol® OT	Anionic	Leinco	K40000	445	13.5
Benzalkonium chloride	Cationic	Leinco	K40000	340	
Brij® 35	Nonionic	Leinco	K40000	1200	16.9
Brij® 98	Nonionic	Leinco	K40000	1150	15
Chemal LA-9	Nonionic	Leinco	K40000	583	13.3
Cremophor® EL	Nonionic	Leinco	K40000	3000	13
IGEPAL® CA-630	Nonionic	Leinco	K40000	603	13
Merpol® A	Nonionic	Leinco	K40000	500	6
Pluronic® F68	Nonionic	Leinco	K40000	8400	24
Pluronic® F-127	Nonionic	Leinco	K40000	12500	20.5
Pluronic® L64	Nonionic	Leinco	K40000	2900	15
Silwet® L-7600	Nonionic	Leinco	K40000	4000	15
Surfactant 10G	Nonionic	Leinco	K40000	-	12.4
Surfynol® 465	Nonionic	Leinco	K40000	700	13
Synperonic® F108	Nonionic	Leinco	K40000	14000	27
Tergitol®	Nonionic	Leinco	K40000	603	17.8
Tetronic® 90R4	Amphotric	Leinco	K40000	7200	4.5
Triton® X-100	Nonionic	Leinco	K40000	625	13.5
Triton® X-305	Nonionic	Leinco	K40000	1526	17.3
Tween® 20	Nonionic	Leinco	K40000	1228	16.7
Tween® 80	Nonionic	Leinco	K40000	1310	15
SDS	Anionic	Sigma-Aldrich	L3771	18000	40
Tergitol™	Nonionic	Sigma-Aldrich	NP40S	600	17.8
IGEPAL® CA-630	Nonionic	Sigma-Aldrich	I8896	603	13
IGEPAL® CA-720	Nonionic	Sigma-Aldrich	238589	660	14
IGEPAL® CO-520	Nonionic	Sigma-Aldrich	238643	603	10
IGEPAL® CO-630	Nonionic	Sigma-Aldrich	542334	643	13
TX-305	Nonionic	Sigma-Aldrich	X305	1620	17.3
Pluornic F-127	Nonionic	Sigma-Aldrich	P2443	12600	20.5
Poloxamer 188	Nonionic	Sigma-Aldrich	P5556	8400	29
Brij® 35	Nonionic	Sigma-Aldrich	8019620250	1199	16.9
Triton® X-405	Nonionic	Sigma-Aldrich	X405	1900	17.6
Surfynol® 465	Nonionic	Sigma-Aldrich	461199	332.5	13
Tween® 20	Nonionic	Sigma-Aldrich	P7949	1228	16.7
Pluronic® L-35	Nonionic	Sigma-Aldrich	435414	1228	20.5
Pluronic® 10R5	Nonionic	Sigma-Aldrich	435473	2000	15
Pluronic® L64	Nonionic	Sigma-Aldrich	435449	2900	15
Pluronic® F108	Nonionic	Sigma-Aldrich	542342	14600	24

Supplementary References

1. WANG, C., WU, J., ZONG, C., XU, J. & JU, H.-X. Chemiluminescent Immunoassay and its Applications. *Chin. J. Anal. Chem.* **40**, 3–10 (2012).
2. Peng, P. *et al.* Emerging ELISA derived technologies for in vitro diagnostics. *TrAC, Trends Anal. Chem.* **152**, 116605 (2022).
3. Li, S. *et al.* Electrochemical Biosensors for Whole Blood Analysis: Recent Progress, Challenges, and Future Perspectives. *Chem. Rev.* **123**, 7953–8039 (2023).
4. Zhu, H. *et al.* PCR Past, Present and Future. *Biotechniques* **69**, 317–325 (2020).
5. Kaisti, M. *et al.* Hand-Held Transistor Based Electrical and Multiplexed Chemical Sensing System. *ACS Sens.* **1**, 1423–1431 (2016).
6. Janićijević, Ž. *et al.* Methods gold standard in clinic millifluidics multiplexed extended gate field-effect transistor biosensor with gold nanoantennae as signal amplifiers. *Biosens. Bioelectron.* **241**, 115701 (2023).
7. Mahmoudi, A., Nazari, K., Mohammadian, N. & Moosavi-Movahedi, A. A. Effect of Mn2+, Co2+, Ni2+, and Cu2+ on horseradish peroxidase. *Appl. Biochem. Biotechnol.* **104**, 81–94 (2003).
8. Xia, Y., Liu, Y., Hu, X., Zhao, F. & Zeng, B. Dual-Mode Electrochemical Competitive Immunosensor Based on Cd2+/Au/Polydopamine/Ti3C2 Composite and Copper-Based Metal–Organic Framework for 17β-Estradiol Detection. *ACS Sens.* **7**, 3077–3084 (2022).
9. Jang, H.-J. *et al.* Radical-mediated electrical enzyme assay for estradiol: Toward point-of-care diagnostics. *Device* **3**, 100807 (2025).
10. Monerris, M. J., Arévalo, F. J., Fernández, H., Zon, M. A. & Molina, P. G. Integrated electrochemical immunosensor with gold nanoparticles for the determination of progesterone. *Sens. Actuators B Chem.* **166–167**, 586–592 (2012).
11. Liang, S. *et al.* Measuring luteinising hormone pulsatility with a robotic aptamer-enabled electrochemical reader. *Nat. Commun.* **10**, 852 (2019).
12. Tang, Z. *et al.* Fluorescence and visual immunoassay of HIV-1 p24 antigen in clinical samples via multiple selective recognitions of CdTe QDs. *Microchimica. Acta* **188**, 422 (2021).
13. Ma, Y., Shen, X.-L., Zeng, Q., Wang, H.-S. & Wang, L.-S. A multi-walled carbon nanotubes based molecularly imprinted polymers electrochemical sensor for the sensitive determination of HIV-p24. *Talanta* **164**, 121–127 (2017).
14. Altın, K. H. & Agel, E. Development of Molecular-Based Screening Test for Hepatitis B Virus in Human Plasma Samples. *Jpn. J. Infect. Dis.* **77**, JJID.2023.313 (2024).